708

AIAA 93-[redacted]

Structure of Soot-Containing Laminar Jet Diffusion Flames

S. Mortazavi, P.B. Sunderland, J. Jurng,
Ü.Ö. Köylü and G.M. Faeth
Department of Aerospace Engineering
The University of Michigan
Ann Arbor, Michigan

31st Aerospace Sciences Meeting & Exhibit
January 11-14, 1993 / Reno, NV

AIAA-93-0708

STRUCTURE OF SOOT-CONTAINING LAMINAR JET DIFFUSION FLAMES

S. Mortazavi,* P.B. Sunderland,* J. Jurng,† Ü.Ö. Köylü**
and G.M. Faeth††
Department of Aerospace Engineering
The University of Michigan
Ann Arbor, Michigan 48109-2140

Abstract

The structure and soot properties of nonbuoyant and weakly-buoyant round jet diffusion flames were studied, considering ethylene, propane and acetylene burning in air at pressures of 0.125-2.0 atm. Measurements of flame structure included radiative heat loss fractions, flame shape and temperature distributions in the fuel-lean (overfire) region. These measurements were used to evaluate flame structure predictions based on the conserved-scalar formalism in con junction with the laminar flamelet concept, finding good agreement between predictions and measurements. Soot property measurements included laminar smoke points, soot volume function distributions using laser extinction, and soot structure using thermophoretic sampling and analysis by transmission electron microscopy. Nonbuoyant flames were found to exhibit laminar smoke points like buoyant flames but their properties are very different; in particular, nonbuoyant flames have laminar smoke point flame lengths and residence times that are shorter and longer, respectively, than buoyant flames. Soot property measurements suggest that these differences are caused by different soot paths in the fuel-rich region, and a much larger soot oxidation region, for nonbuoyant than buoyant flames.

Nomenclature

d	=	burner exit diameter
d_p	=	primary soot particle diameter
f	=	mixture fraction
f_v	=	soot volume fraction
g	=	acceleration of gravity
L	=	flame length
n_a	=	number of aggregates per unit volume
n_p	=	number of primary particles per unit volume
N	=	number of primary particles in an aggregate
p	=	pressure
r	=	radial distance
Re	=	burner exit Reynolds number, $u_o d/\nu_o$
t_r	=	residence time
T	=	temperature
u	=	streamwise velocity
$\mathbf{u}$	=	velocity vector
v	=	radial velocity
z	=	streamwise distance
μ	=	molecular viscosity
ν	=	kinematic viscosity
ρ	=	density
σ	=	Prandtl/Schmidt number
ϕ	=	fuel-equivalence ratio

Subscripts

o	=	burner exit condition
∞	=	ambient condition

Superscripts

$\overline{()}$	=	average over aggregate population
$()^T$	=	transpose of a tensor

Introduction

The scalar structure and soot properties of round laminar jet diffusion flames were studied in order to gain a better understanding of soot formation, growth, aggregation, oxidation and radiative properties within nonpremixed flames. Soot properties in nonpremixed flames are important because they affect the performance of propulsion systems, the hazards of unwanted fires, and pollutant emissions from combustion processes. Although the properties of soot within turbulent flames are of the greatest practical interest, the present investigation was limited to laminar flames where detailed measurements are more tractable. Attention was confined to either weakly-buoyant flames at low pressures in normal gravity (ng) or nonbuoyant flames at normal pressures in microgravity (μg). This was done in order to investigate the differences between soot properties in nonbuoyant diffusion flames and the more widely studied buoyant diffusion flames, and to evaluate whether either flame system provides an appropriate model of soot processes in practical turbulent flames. The measurements also were used to evaluate predictions of flame structure because they could provide estimates of the environment of soot processes for conditions where detailed structure measurements are not feasible.

A number of investigators have considered the structure of nonbuoyant laminar diffusion flames, using drop towers to provide a μg environment.[1-8] Quantitative measurements have been limited to flame lengths, with good agreement found between predictions based on the conserved-scalar formalism and measurements. Unfortunately, flame length is not a very sensitive indicator of model performance.[9] Additionally, the limited instrumentation and time capabilities of drop towers have prevented detailed studies of soot properties within nonbuoyant laminar diffusion flames.

In contrast, numerous studies of the structure and soot properties of buoyant laminar diffusion flames have been reported, see Glassman[10] for a recent review of work in the field. A popular configuration for these studies has been coflowing laminar jet diffusion flames that typically are used for measurements of laminar smoke point properties.[11] Among others, Santoro and Dobbins and coworkers have extensively studied this configuration at atmospheric pressure,[12-18] while Flower and Bowman[19,20] have considered effects of ambient pressure. However, buoyancy causes soot to be confined to a narrow soot layer that is difficult to resolve experimentally, while the path that soot follows as it grows and oxidizes is completely different in

---

* Graduate Student Research Assistant.
† Visiting Research Fellow, currently with KAIST, Seoul,Korea.
** Research Fellow.
†† Professor, Fellow AIAA.

buoyant and nonbuoyant flames, e.g., soot nucleation occurs near the flame sheet for buoyant flames but in the cooler core of the flow for nonbuoyant flames. This raises questions about the relevance of findings for buoyant laminar flames to nonbuoyant flames which generally are of greatest practical interest. Additionally, Glassman[10] questions the existence of global soot properties like laminar smoke point flame lengths for nonbuoyant diffusion flames, analogous to buoyant flames, because nonbuoyant flames have residence times that are independent of flame length under the boundary layer approximations. Whether this is true clearly is of interest, as are the differences between soot properties within nonbuoyant and buoyant flames.

Finally, detailed simulations of chemical kinetics have been successful for predicting the structure of methane/air flames where soot concentrations are relatively low.[21,22] However, analogous methods for soot-containing flames will require substantial advances in the understanding of fuel decomposition and soot chemistry, while the computational tractability of such methods for practical flames is questionable. An attractive alternative involves the use of the conserved-scalar formalism, in conjunction with state relationships for scalar properties as a function of mixture fraction (called the laminar flamelet approach), as proposed by Bilger.[23] In particular, measurements in soot-containing laminar diffusion flames show that state relationships for major gas species are relatively universal for a particular fuel type for combustion in air.[23-25] Furthermore, generalized state relationships have been found for a wide variety of hydrocarbon/air flames.[26] Thus, there appears to be potential for predicting the structure of laminar diffusion flames while avoiding both the uncertainties and complexities of detailed models of the chemistry of soot-containing environments, using the laminar flamelet approach. However, the accuracy and limitations of predictions based on the laminar flamelet approach have not been evaluated.

In view of this status, the present investigation had two main objectives, as follows: (1) to complete measurements of the structure of soot-containing laminar diffusion flames in order to evaluate structure predictions based on the laminar flamelet approach, and (2) to complete measurements of soot properties in both weakly-buoyant and nonbuoyant laminar diffusion flames. Present measurements included flame shapes, temperature distributions, radiative heat loss fractions, soot concentrations and soot structure properties in weakly-buoyant flames, and laminar smoke point flame lengths and residence times in nonbuoyant flames. Measurements were limited to laminar round jet diffusion flames burning in still air. The weakly-buoyant flames involved ethylene and acetylene at ambient pressures in the range 0.125-0.250 atm, while the nonbuoyant flames involved ethylene and propane at pressures in the range 0.5-2.0 atm.

Flame Structure

Experimental Methods

Test Apparatus. The present measurements of both flame structure and soot properties involved weakly-buoyant flames at ng. These experiments exploit the fact that buoyancy scales like p^2g in laminar flames.[9] Thus, flames at pressures on the order of 0.1 atm have effective gravitational levels on the order of 0.01g, in comparison to flames at atmospheric pressure, and are weakly-buoyant if they are not too large. Thus, present measurements involved test flames from 3 mm diameter burners that had luminous regions that generally extended less than 50 mm from the burner exit. The ambient pressure range of the tests was 0.125-0.250 atm, which provided a reasonable compromise between reduced soot concentrations at low pressures and increased effects of buoyancy at high pressures.

The test configuration involved a round fuel jet injected vertically upward, surrounded by a slow concentric flow of air. The flames burned along the axis of a vertical cylindrical enclosure having diameter and length of 300 mm. The top and bottom of the enclosure were porous metal plates which separated the enclosure from plenum chambers for air inflow and exhaust outflow, which provided a uniform distribution of air flow over the enclosure crossection. Additional air was admitted to the upper plenum chamber to control the temperature of the exhaust flow. Air inflow was measured with a rotameter operating at atmospheric pressure before passing through a pressure regulator to the air inlet plenum. The rotameter was calibrated using a wet test meter. The exhaust flow was removed using a vacuum pump.

The fuel flow port was aligned with the axis of the test enclosure with its exit 50 mm above the lower porous plate. The inside diameter of the fuel port was 3 mm, with outside surface chamfered at an angle of 30° at the exit in order to minimize disturbances of the entrained air flow into the flames. The fuel flow passage had a flow straightener at the inlet followed by a constant area passage having a length-to-diameter ratio of 20:1 to yield fully-developed laminar pipe flow at the burner exit. The fuel flow was measured using a rotameter operating at atmospheric pressure before passing through a pressure regulator to the fuel inlet plenum. The flames were ignited with a hot wire coil that could be placed near the burner exit and then rotated to a position near the chamber wall once the flames were ignited and stabilized.

The flames were observed using four 110 mm diameter fused quartz windows located at 90° intervals around the side walls of the chamber. The axis of these windows was roughly 25 mm above the exit of the fuel port, which roughly centered the flames on the windows. The entire test chamber could be traversed in the vertical and horizontal directions in order to accommodate rigidly mounted optical instrumentation. Horizontal traversing was carried out using a stepping motor driven linear positioner with a positioning accuracy of 5 μm. Vertical traversing was carried out using a heavy duty laboratory jack with a manual positioning accuracy of 0.5 mm.

Instrumentation. Instrumentation included still photography for measurements of flame shape, thermocouples for measurements of temperature distributions in the fuel-lean region of the flames, and a radiation heat flux transducer for measurements of the radiative heat loss fractions of the flames. The still photographs were taken in a darkened room using a 35 mm single lens reflex camera. The camera was directed through one of the side windows and had a field of view of 80 mm and a depth of field of 40 mm, which was sufficient to cover the luminous region of the flames. Color film was used so that yellow soot luminosity could be distinguished from the blue luminosity associated with the position of the flame sheet. The films were processed to yield 100 × 125 mm color images which were used directly for measurements of flame shapes. The outlines of the blue and yellow regions

could be measured with an accuracy of 0.5 mm.

The test flames were not soot emitting so that it was possible to use bare wire thermocouples to measure temperatures in the region above the luminous soot-containing region. The thermocouple probe involved a horizontal rake passing through the axis of the flow with five thermocouple junctions spaced 15 mm apart in the radial direction. The rake could be located at three radial positions to provide measurements 5 mm apart. Chromel-alumel thermocouples having a wire diameter of 50 μm were used for the measurements. The lead wires to the junctions were aligned with the streamwise direction and extended more than 100 wire diameters to their mounting point in order to minimize conduction errors. Predictions of the flame structure, which proved to be reasonably accurate, were used to correct the thermocouple readings for radiation errors. These corrections were relatively small (less than 30 K) due to relatively low temperatures at conditions where measurements were made (less than 1150 K). Overall experimental uncertainties of the temperature measurements (95% confidence) are estimated to be less than 5% of the temperature difference between the flow and the ambient environment.

The total radiative power of the flames was measured using a wide-angle heat flux transducer (Medtherm, Model 64P-0.2-22) that viewed the flames through one of the observation windows. For these measurements, the regular window was replaced with a 50 mm diameter × 8 mm thick calcium fluoride window having a transmittivity of 94% for the wavelength range 400-7500 nm. The included angle of the length of the visible portion of the flames from the detector was less than 15° so that cosine errors were less than 1%. The total radiative power was found assuming spherically isotropic radiant flame emission. This is a good approximation for present conditions because each element of the flame radiates isotropically while effects of reabsorption of radiation are small for the present optically-thin flames.[27] The radiative heat loss function was then found from the known fuel flow rate and the lower heat of combustion of the fuel.

Theoretical Methods

The predictions of flame structure were based on the following major assumptions: steady laminar axisymmetric flow; constant radiative heat loss fraction of the chemical energy release for all parts of the flame; the laminar flamelet approximation for all scalar properties, which requires the previous radiation approximation and implies equal binary diffusivities of all species, negligible thermal diffusion and unity Lewis number; small flame standoff distance at points of flame attachment; ambient environment has constant properties; ideal gas mixtures with negligible soot volumes and a constant Prandtl/Schmidt number; and multicomponent mixing laws to find the mixture viscosity. Steady laminar axisymmetric flow is a condition of the experiment while the other approximations all are aspects of the laminar flamelet approach which is being tested.[23-26] State relationships for the gas species for the ethylene and acetylene/air flames were drawn directly from Gore and Faeth.[24,25] These results are for atmospheric pressure diffusion flames but were applied to the low pressure flames as well for lack of an alternative. The state relationships for temperature were computed given the known state relationships for major gas species and the radiative heat loss fraction, as described by Sivathanu and Faeth.[26] Edelman and Bahadori[5] demonstrated the importance of streamwise diffusion for Re < 100, which includes present test conditions; therefore, the full elliptic governing equations were solved rather than adopting the boundary layer approximations.

Based on these assumptions, the governing equations for the flames are as follows:

$$\nabla \cdot (\rho \mathbf{u}) = 0 \qquad (1)$$

$$\nabla \cdot (\rho \mathbf{u}\mathbf{u}) = \rho \mathbf{g} - \nabla p - \nabla \cdot (\mu(\nabla \mathbf{u} + \nabla \mathbf{u}^T)) \qquad (2)$$

$$\nabla \cdot (\rho \mathbf{u} f) = \nabla \cdot (\mu \nabla f)/\sigma \qquad (3)$$

The boundary condition across the burner exit involved fully-developed laminar pipe flow with f=1, by definition. Two limiting cases were considered for the remaining boundary conditions: a slow coflow of air for the weakly-buoyant flame experiments, or no-slip boundary conditions for the enclosure geometry for the nonbuoyant flame conditions. The effect of coflow was small, generally less than 1% along the axis, for coflow velocities up to 10% of the burner exit velocity. The equations were solved following Patankar,[28] with a variable grid spacing and a 60 (radial) × 88 (streamwise) mesh. Computations for various grid sizes indicated numerical accuracy within 1-2% by Richardson extrapolation

Results and Discussion

Flame Shapes. Initial evaluation of the predictions involved comparison of predicted and measured flame shapes. The predicted locations of the flames were taken to be the locus of the stoichiometric mixture fraction. An example of flame length predictions and measurements for nonbuoyant laminar jet diffusion flames is illustrated in Fig. 1. The flame length measurements are from Haggard and Cochran[2] for ethylene/air flames at atmospheric pressure and μg conditions. Similar to most other evaluations of flame lengths for moderately sooting fuels,[9] the comparison between predictions and measurements is excellent. While this is promising, however, it is not definitive due to the relative insensitivity of flame length predictions to variations of model properties.[9]

Typical flame shape predictions and measurements for weakly-buoyant laminar jet diffusion flames from the present investigation are illustrated in Fig. 2. These results are for ethylene/air flames at ambient pressures of 0.125 and 0.250 atm with burner exit Reynolds numbers of 25, 50, 100 and 120. Findings were similar for the acetylene/air flames over a comparable range of conditions. The experimental results denote the position of the boundary of the blue portion of the flame; these measurements are terminated in the region where yellow luminosity from soot prevents observation of the blue boundary. Effects of buoyancy, ambient pressure and coflow are relatively weak, only reducing flame lengths slightly from the behavior illustrated in Fig. 1 at μg. Thus, the main effect of reduced ambient pressures is to increase the maximum width of the flames and to increase the region where the blue boundary can be observed due to lower soot concentrations at lower pressures. The comparison between predictions and measurements is reasonably good, including proper treatment of the effects of burner exit Reynolds numbers on flame shapes and the tendency of the flames to attach somewhat below the exit of the burner due to streamwise diffusion.

Temperature Distributions. Predicted and measured temperature distributions in the fuel-lean region of weakly-buoyant laminar jet diffusion flames are illustrated in Fig. 3. These results involve ethylene/air flames at 0.25 atm with burner exit Reynolds numbers of 25, 50 and 100. Findings at other conditions, however, were similar. The comparison between measured and predicted temperatures is seen to be reasonably good. The main deficiencies of predictions are a slight overestimation of peak temperatures and underestimation of flow widths, which could be caused by slight disturbances of the flame due to gas motion within the test enclosure.

Discussion. Taken together, the results illustrated in Figs. 1-3 suggest potential for use of the conserved-scalar formalism, in conjunction with the laminar flamelet concept, to estimate the structure of soot-containing flames. However, additional evaluation of the method is needed to establish this approach. For example, effects of pressure on state relationships, and predictions of scalar properties and velocities within the luminous, soot-containing region of the flames, still must be evaluated.

Laminar Smoke Point Properties

Experimental Methods

Apparatus. Measurements of the laminar smoke point properties of nonbuoyant laminar jet diffusion flames were carried out using the NASA KC-135 μg facility. This aircraft flies parabolic trajectories that provide roughly 20s at low gravity conditions. These experiments involved ethylene and propane flames burning in air, or slightly vitiated air (10% maximum oxygen consumption by volume), within a closed windowed chamber. The chamber was cylindrical with an internal volume of roughly 87 liters. The chamber volume can be nearly evacuated by venting overboard, due to the altitude of the aircraft, and was refilled with air stored in compressed cylinders in order to control levels of vitiation. The chamber was fitted with two windows and an interior light for laminar smoke point measurements. The chamber pressure was measured using an absolute pressure gage.

Three round burners were considered during the tests, having inside diameters of 1.6, 2.7 and 5.9 mm. Other features of these burners were similar to the weakly-buoyant flame tests discussed earlier. Fuel was delivered from storage bottles through a solenoid valve, a needle metering valve and a mass flow rate meter to the plenum of the fuel port. The flames were ignited using a retractable hot wire coil, similar to the weakly-buoyant flame tests.

Instrumentation. The appearance of the flames was recorded with a video camera. This allowed subsequent determination of disturbed flames, due to departures from the parabolic flight path, so that observations at these conditions could be eliminated from the data. The video records also were used to measure flame lengths, which were taken to be the visible luminous portion of the flames. This involved averaging over a 3-5s period toward the end of the low-gravity period when fully-developed flame shape conditions were reached. Estimated experimental uncertainties (95% confidence) of the flame length determinations were less than 2 mm.

Only one flame condition was considered during each low-gravity parabola so that steady conditions could be reached. During each parabola, the fuel flow rate, the chamber pressure and the soot emission condition of the flame, were recorded orally using the audio channel of the video record. The flame lengths recorded at the onset of sooting conditions were actually flame luminosity lengths, which is similar to the laminar smoke point flame lengths definition conventionally used for buoyant laminar jet diffusion flames.[11] However, unlike buoyant flames, luminosity lengths for the present nonbuoyant flames are appreciably longer than flame lengths based on the location of the stoichiometric mixture fraction, at the flame axis. This comes about due to the extended soot oxidation region of nonbuoyant flames which will be discussed in more detail later. Based on the accuracy of flame length determinations, and the range of conditions between observations of nonsooting and sooting flames, the experimental uncertainties (95% confidence) of smoke point flame luminosity lengths are estimated to be less than 10%.

Theoretical Methods

Laminar smoke point residence times are a useful parameter for characterizing the sooting properties of a fuel, in addition to laminar smoke point flame lengths. This is particularly true for nonbuoyant flames where effects of streamwise diffusion cause residence times to vary considerably for a given flame length, in contrast to buoyant flames where flame lengths and residence times are closely correlated.[29,30] Past work with buoyant flames at ng has involved direct measurements of laminar smoke point residence times, taken as the time between the termination of fuel flow at the burner exit and the disappearance of all flame luminosity.[29,30] Similar measurements of residence times were not available for the present μg tests; therefore, they were computed using the flame structure model discussed earlier. For these computations, the characteristic flame residence time was defined as the time required for a fluid parcel to convect along the axis from the burner exit to the flame sheet, i.e., to the condition where the stoichiometric mixture fraction is reached at the flame axis.

Typical predictions of characteristic flame residence times for nonbuoyant ethylene/air flames at atmospheric pressure are illustrated in Figs. 4 and 5. Effects of fuel type on residence times are small so that findings for other fuels are essentially the same. The results illustrated in Fig. 4 show that increasing flame lengths for a fixed burner exit diameter yield progressively increasing residence times. This is similar to the behavior of buoyant flames at ng where residence times are proportional to the square root of the flame length.[10,29,30] However, it differs from simple constant property estimates of residence times for nonbuoyant flames based on the boundary layer approximations, where residence times are independent of the burner flow rate and only vary with the burner diameter.[31] This difference primarily is caused by effects of streamwise diffusion.

The results illustrated in Fig. 5 show that residence times progressively increase with increasing burner exit diameter if the flame length is kept constant at 45 mm (which is typical of conditions used for the present soot property measurements). This behavior is expected from simplified treatments of nonbuoyant laminar jet diffusion flames; it is caused by reduced flow velocities at the burner exit as the burner diameter is increased for a fixed flame length.[31] This behavior is in sharp contrast to buoyant laminar jet diffusion flames at ng, where the residence time largely is a function

of flame length and is relatively independent of burner diameter and exit velocity because buoyancy controls flow velocities except for very short flames.[29,30]

Two other features of the residence time computations are helpful for interpreting measurements of soot properties within nonbuoyant laminar jet diffusion flames. First of all, the results illustrated in Figs. 4 and 5 indicate that residence times for nonbuoyant flames are much larger than those of buoyant flames of comparable length, e.g., 2400 ms at μg in comparison to roughly 50 ms at ng for burner diameters of 10 mm and flame lengths of roughly 50 mm (the 10 mm diameter is typical of measurements at ng).[10,29,30] Finally, residence times for nonbuoyant flames are proportional to pressure for a given burner exit diameter and flame length.

Results and Discussion

Smoke Point Luminosity Lengths. Table 1 is a summary of laminar smoke point luminosity lengths measured for round laminar jet diffusion flames at both μg and ng. Present results at μg are for ethylene and propane/air flames at pressures of 0.5, 1.0 and 2.0 atm and burner exit diameters of 1.6, 2.7 and 5.9 mm. The results at ng are from Refs. 11 and 29 and are for ethylene and propane/air flames at atmospheric pressure with a burner exit diameter of roughly 10 mm (results at ng are relatively independent of burner diameter).[29,30]

There are several interesting features of the results summarized in Table 1. First of all, the nonbuoyant flames exhibit laminar smoke point luminosity lengths, in contrast to the conjecture of Glassman[10] that this behavior would not be observed because nonbuoyant flames have residence times that are independent of flame length under the boundary layer approximations. This behavior does not occur due to streamwise diffusion so that increasing flame lengths provide increasing residence times that lead to conditions where the flames emit soot, as discussed in connection with Fig. 4. Next, the nonbuoyant flame measurements exhibit relatively little effect of burner diameter on smoke point luminosity lengths, which is similar to behavior observed at ng.[30] This behavior is expected at ng where residence times largely are a function of the flame length, however, it was not expected at μg where residence times increase with increasing burner diameter for a given flame length, see Fig. 5. Next, smoke point luminosity lengths are appreciably shorter at μg than ng, roughly four times shorter and even shorter if the differences between luminosity and flame lengths at μg are considered. On the other hand, laminar smoke point residence times are much longer at μg than ng, e.g., 200-1500 ms at μg based on the results illustrated in Figs. 4 and 5, in comparison to 40-50 ms for the same fuels at ng.[29] However, other properties of the laminar smoke point luminosity lengths are qualitatively similar at μg and ng: smoke point luminosity lengths increase with decreasing pressure and are slightly longer for propane than ethylene.

Discussion. The reasons for the differences between the smoke point properties of laminar jet diffusion flames at μg and ng certainly are not understood at present. However, two general phenomena probably play a role in this behavior: one involving the motion of soot through the flame, the other involving flame structure. In particular, the path of soot particles after they first form until they cross the flame sheet, in mixture fraction space, is completely different. For nonbuoyant flames, soot first forms at fuel-rich conditions in the cool core of the flow and then moves directly toward the flame sheet, experiencing a monotonic reduction of mixture fraction. In contrast, for buoyant flames, soot first forms near the flame sheet and is drawn toward fuel-rich conditions initially before reversing direction in mixture fraction space and finally passing through the flame sheet again,[12,13] because the dividing streamline of the flow lies inside the flame sheet throughout most of the fuel-rich region.[9]

Differences in the structure of nonbuoyant and buoyant flames provide another mechanism for different sooting properties. In particular, flow velocities and gradients in scalar properties progressively decrease with increasing distance from the burner exit for nonbuoyant flames, which provides an extended soot oxidation region with relatively large local residence times due to the low flow velocities. In contrast, flow velocities progressively increase with the corresponding flame stretch tending to increase gradients of scalar properties for buoyant flames, which promotes quenching of soot oxidation reactions and limits the extent of the soot oxidation region.

In view of these differences in soot paths and flow structure it certainly is not surprising that the soot emission properties of nonbuoyant and buoyant flames are different. Additionally, it is clear that nonbuoyant jet diffusion flames provide an interesting new perspective to gain a better understanding of soot mechanisms in diffusion flame environments.

Soot Properties

Experimental Methods

Apparatus. Soot properties were measured in weakly-buoyant laminar jet diffusion at ng. This involved observations of flames at low ambient pressures using the apparatus described in connection with evaluation of the flame structure predictions. Present experiments, however, were limited to acetylene/air flames in order to obtain reasonable concentrations of soot at low pressures by using a heavily sooting fuel like acetylene.

The specific test conditions for soot property measurements are summarized in Table 2. Three pressures were considered — 0.125, 0.188 and 0.250 atm — with burner exit conditions adjusted to give luminous flame lengths of roughly 60 mm. This required slightly increasing burner exit Reynolds numbers as pressures were reduced. The lower soot concentrations at lower pressures is reflected by lower radiative heat loss fractions due to reduced continuum radiation from soot.

Instrumentation. Methods for observing flame shapes and temperature distributions at fuel-lean conditions were the same as for the flame structure experiments discussed earlier. Thus, only methods for measuring soot concentrations and structure will be discussed in the following.

Soot concentrations were measured using laser extinction following methods used earlier in this laboratory.[24,25] This involved deconvoluting laser-extinction measurements for various chord-like paths through the flames in order to obtain radial profiles of soot volume fractions. Extinction was measured by focusing a helium-neon laser beam (5 mW of optical power at 632.8

nm) at a plane through the flame axis to yield a beam diameter of 250 μm with a confocal length of 30 mm, so that the constant diameter portion of the beam extended through the soot-containing region of the flames. The laser beam was mechanically chopped at a frequency of 500 Hz, which provided adequate control of flame luminosity in conjunction with carrier amplification of the detector signal and a laser line filter before the detector. The optical power of the beam was measured before and after passing through the flames, with independent scans when the flame was not present to correct for absorption by the windows of the apparatus. The extinction measurements were analyzed assuming scattering at the small particle (Rayleigh) scattering limit. A recent investigation indicates that enhanced scattering from soot at present conditions causes the Rayleigh scattering approximation to overestimate soot volume fractions by less than 20% for present conditions, which is small in comparison to potential errors due to the uncertainties of the refractive indices of soot.[32-34] The computations of soot volume fractions were based on the refractive indices of Dalzell and Sarofim[35] in order to be consistent with earlier work.[12,24,25] Recent measurements of soot scattering properties also support use of these refractive indices in comparison to other results in the literature.[34] Individual extinction measurements were integrated over a 1s interval to minimize effects of noise, with 40 extinction paths separated by 0.5 mm for each deconvolution. Results from 10 separate scans and deconvolutions were used to obtain final soot volume fraction distributions. Uncertainties of refractive indices over the existing range of reported values could yield a variation of soot volume fractions of up to 25%.[32] Other experimental uncertainties (95% confidence) are estimated to be less than 15% for soot volume fractions greater than 0.1 ppm, increasing inversely proportional to soot volume fractions at lower soot volume fractions.

The structure of soot was measured by thermophoretic sampling and analysis using transmission election microscopy (TEM) similar to Dobbins and Megaridis,[14] but following specific methods of Köylü and Faeth.[36] The sampling surfaces were 3 mm diameter copper grids used to hold TEM specimens (200 mesh copper grids supported by 20 nm thick elemental carbon film). The grids were aligned in the vertical direction, parallel to the mean flow direction, and centered on the flame axis during sampling. The grids were mounted on a 3 × 5 mm metal strip using double-backed adhesive which was mounted in turn on a retractable probe. The probe was stored in a cylinder with roughly a 50 mm stroke to reach the flame axis. A double-acting pneumatic cylinder rapidly drove the probe out of the storage cylinder to the sampling position and returned it to the cylinder again when sampling was complete. Sampling times were controlled so that no more than 10% of the surface of the TEM grid was covered with soot aggregates to prevent overlapping aggregates on the grid. This required 30-60 ms sampling times, in comparison to 2-3 ms traveling times of the grid through the flame to the axis. The mounting point of the sampling system was varied to accommodate measurements at various distances from the burner exit.

The principles of thermophoretic sampling are discussed elsewhere[14,36,37] In particular, the results of Rosner et al.[37] show that effects of aggregate size cause negligible sampling bias for present test conditions. The details of TEM analysis were identical to Köylü and Faeth.[36] The experimental uncertainties of directly measured soot structure parameters (95% confidence) are as follows: mean primary particle diameters less than 5% and mean number of primary particles per soot aggregate less than 20%. The mean number of primary particles and aggregates per unit volume were computed from the measured mean soot volume fraction and structure properties as follows:

$$\bar{n}_p = \bar{N}\,\bar{n}_a = 6\,\bar{f} / (\pi\,\bar{d}_p^3) \qquad (4)$$

Based on the uncertainties of $\bar{f}$ and $\bar{d}_p$, the experimental uncertainties (95% confidence) of $\bar{n}_p$ and $\bar{n}_a$ are less than 21 and 29%, respectively, for soot volume fractions greater than 0.1 ppm.

Results and Discussion

Flame Structure. Plots of the measured blue flame-sheet and yellow soot-luminosity boundaries are illustrated in Fig. 6. The predicted locations of the flame sheet from the flame structure analysis, taken as the locus of the stoichiometric mixture fraction, also are shown on the plots. Although the luminosity lengths of the three flames are similar, the estimated flame lengths (based on stoichiometric conditions at the flame axis) increase as the pressure decreases, due to increasing burner exit Reynolds numbers as the pressure decreases, see Table 2. Predicted flame boundaries are reasonably good at 0.250 atm., similar to earlier results discussed in connection with Fig. 2 for ethylene/air flames. However, the predictions progressively overestimate flame widths as pressure decreases. Specific reasons for this behavior are unknown, although the present approximate treatment of flame radiation and transport properties are likely areas where improvements are needed.

The region of soot luminosity lies inside the flame sheet near the jet exit, but subsequently extends well beyond the locus of the stoichiometric mixture fraction: this highlights the extended soot oxidation region of nonbuoyant flames. The small "ears" near the end of the soot luminosity region also are observed in buoyant flames,[11] they result from the larger soot concentrations that develop in the soot layer near the flame sheet. This soot layer also is responsible for the apparent close approach of soot luminosity to the exit of the flame in the present projected images: this luminosity actually originates from the soot layer near the flame sheet at some distance from the cool fuel gas leaving the burner exit.

Soot concentrations. Typical radial distributions of soot volume fractions are illustrated in Fig. 7. These results are for the acetylene/air flame at 0.250 atm. An annular soot layer is quite evident near the burner exit, with soot building up later near the axis as the flame tip based on stoichiometric conditions at the axis is approached (estimated to be at z/d = 7-9). Soot oxidation extends to the axis beyond the flame tip with soot concentrations becoming small at all radial distances far from the burner exit in this nonsooting flame. The breath of the soot-containing region, and its uniformity far from the burner exit, provides unprecedented spatial resolution for studying soot processes in comparison to ng conditions at atmospheric pressure.

The soot layer seen in Fig. 7 is a result of soot nucleation and growth at fuel-rich conditions followed by soot oxidation at fuel-lean conditions. Near the tip of the flame, effects of thermophoresis are small for present conditions and flow velocities cross the flame sheet from fuel-rich to fuel-lean conditions. Then, as temperature increases as the flame sheet is approached along a streamline (or soot pathline), soot nucleation and growth cause soot

concentrations to increase and reach a maximum near the flame sheet. Subsequently, soot oxidation proceeds in the fuel lean region so that soot concentrations become small once again. Soot processes in the lower portions of nonbuoyant flames, however, probably behave somewhat similar the buoyant flames.[9] In this region, entrainment causes the flow to cross the flame sheet from fuel-lean to fuel-rich conditions while effects of thermophoresis inhibit the motion of soot toward the flame sheet. Then soot nucleation begins near the flame sheet with subsequent growth as the flow along a soot pathline moves toward fuel-rich conditions for a time.

The behavior of soot concentrations along soot pathlines for motion monotonically toward fuel lean conditions is illustrated in Fig. 8. This involves plots of soot volume fractions along the axis of all three flames. The effect of pressure on soot concentrations is substantial, with maximum soot volume fractions roughly proportional to p^2 for present test conditions. This strong effect of pressure is reasonable because reduced pressures reduce both soot formation rates and flame residence times. Peak soot concentrations are associated with z/d in the range 7-9, tending to increase with decreasing pressure. This behavior is consistent with peak soot concentrations being reached near stoichiometric conditions, see Fig. 6.

Soot Structure. The structure of the soot observed in the present weakly-buoyant flames was generally similar to earlier observations in buoyant flames.[14,34,36] This involved nearly spherical primary particles collected into wispy aggregates. An exception involved aggregates observed near the end of soot oxidation which were very compact so that it was difficult to resolve individual primary soot particles. These conditions involved very small soot volume fractions, however, and will not be given further consideration here.

The soot structure parameters along the axis of the acetylene/air flame at 0.25 atm. are illustrated in Figs. 9 and 10. Figure 9 is a plot of the directly measured soot structure parameters, $\bar{N}$ and $\bar{d}_p$, while Fig. 10 is a plot of the derived soot aggregate properties, $\bar{n}_p$ and $\bar{n}_a$. The position of the tip of the flames, computed from the structure analysis as the point where the stoichiometric mixture fraction is reached along the axis, also is shown on the plots for reference purposes. Many of the general features of these results can be anticipated from earlier studies of buoyant flames.[12-18] However, aspects of the variation of $\bar{d}_p$ with distance along a soot pathline differ as a result of initial soot nucleation in a relatively cool fuel-rich region as opposed to the region near the flame sheet, as discussed subsequently.

The mean number of soot particles per aggregate, $\bar{N}$ in Fig. 9, generally increases along a soot pathline over the region of the present measurements. This is expected due to processes of aggregation. The region closest to the burner exit exhibits somewhat lower apparent aggregate growth rates with distance for two reasons. First of all, this region involves rather large nucleation rates of new primary particles and the appearance of new aggregates, as indicated by the results plotted in Fig. 10, so that these new smaller particles tend to decrease the overall mean size of the aggregate population. Secondly, gas velocities in this region are largest for nonbuoyant flames so that local residence times are relatively small, tending to reduce aggregate size growth rates in comparison to larger distances from the burner exit. However, it should be noted that the soot inception region was not observed over the present range of measurements, and rates of aggregation are likely to be rather high in this region due to large numbers of individual primary particles, e.g., $\bar{N} \approx 40$, at the first point observed. The region toward the downstream end of the soot-containing region also exhibits lower apparent rates of aggregation in spite of relatively large local residence times and the absence of soot nucleation. This is caused by lower aggregation rates and continued dilution of the flow due to mixing. However, processes of soot oxidation probably also complicate the properties of aggregate size in this region: tending to eliminate some aggregates and to create others as portions of the aggregate structure are oxidized away.

The final reduction of $\bar{d}_p$ with increasing distance from the burner in the soot oxidation region is expected (see Fig. 9) with the large extent of this region being the main difference between nonbuoyant and buoyant flames as noted earlier. However, the initial maximum of $\bar{d}_p$, well before the flame tip is reached, differs from buoyant flames where most soot nucleates near the flame sheet. This behavior probably comes about due to variations in the relative rates of soot nucleation and growth as the flame sheet is approached. Initially, it appears that growth rates at lower mixture fractions are large in comparison to nucleation rates causing rapid growth of the relatively few primary soot particles that are present. However, as fuel concentrations decrease and flow temperatures increase, nucleation rates appear to become more dominant than growth rates, yielding large numbers of smaller primary particles that tend to reduce d_p for the population as a whole, e.g., note the large increase in $\bar{n}_p$ in the region where $\bar{d}_p$ shows an abrupt reduction in the range z/d = 4-6. The local minimum in $\bar{d}_p$ coincides with conditions where $\bar{n}_p$ is a maximum, however, variations of $\bar{d}_p$ within the region of the minimum are within experimental uncertainties so that the relevance of the minimum is questionable. Additionally, the early appearance of a maximum $\bar{d}_p$ may be an artifact of acetylene/air flames due to the role that acetylene plays in soot nucleation and growth;[10] thus, results similar to Fig. 9 for other fuels would be of interest.

Initially, both $\bar{n}_p$ and $\bar{d}_p$ increase with increasing distance from the burner exit, see Fig. 10. However, concentrations of primary particles reach a maximum at fuel-rich conditions and subsequently exhibit a slow decrease. This comes about due to the depletion of soot producing species as the flame sheet is approached, along with effects of continued dilution of the flow as mixing proceeds. The final stages of oxidation are not captured by the results illustrated in Fig. 10 but this region is likely to involve a rather abrupt reduction of $\bar{n}_p$ as primary particles are oxidized away because primary particles are nearly the same size (aside from the relatively small fraction of unusually large particles formed near soot inception conditions). Aggregate concentrations generally parallel primary particle concentrations but growth rates are reduced while decay rates are increased due to the progressive increase of $\bar{N}$ caused by aggregation.

Conclusions

The structure and soot properties of nonbuoyant and weakly buoyant round laminar jet diffusion flames have been studied. The major conclusions of the investigation are as follows:

1. The conserved-scalar formalism, in conjunction with the laminar flamelet concept for scalar properties. appears to be attractive for predicting the structure of soot-containing flames. These predictions require consideration of both radial and streamwise transport, and are very sensitive to estimates of temperature distributions due to the strong sensitivity of transport properties to temperature. Thus, more reliable methods will require improved methods for treating effects of radiative transport — particularly continuum radiation from soot.

2. Nonbuoyant flames exhibit laminar smoke points, and the propensity of a fuel to soot (evidenced by variations of the laminar smoke point luminosity length with fuel type and pressure) is similar for nonbuoyant and buoyant flames. However, laminar smoke point luminosity lengths are much shorter, and laminar smoke point residence times are much longer, for nonbuoyant than buoyant flames.

3. Nonbuoyant flames exhibit broader soot-containing regions, and much larger soot oxidation regions, than buoyant flames of comparable size. Thus, in addition to potentially greater relevance with respect to practical applications, nonbuoyant flames are more convenient than buoyant flames for studies of soot processes in diffusion flames.

4. Present observations of soot structure in nonbuoyant diffusion flames were generally similar to observations in buoyant diffusion flames, with soot consisting of nearly spherical primary particles collected into wispy aggregates. With increasing distance along the flame axis, the number of primary particles per aggregate progressively increased until the final stage of oxidation was reached. Primary particle diameters exhibited more complex behavior, however, reaching a maximum before maximum soot concentrations were reached that suggests a stronger temperature dependence for nucleation than growth rates. The final stages of soot oxidation involved relatively compact aggregates that appear to be the remnant of aggregates consisting of large diameter primary particles formed early to the soot-containing region.

Acknowledgments

This research was sponsored by NASA Grant No. NAG3-1245, under the technical management of D.L. Urban of the Lewis Research Center. The assistance of D.J. Gotti, J.B. Mullins, H.D. Ross, R.G. Sotos, D.P. Stocker and D.L. Urban in carrying out the flame tests using the NASA KG-135 μg test facility is gratefully appreciated.

References

[1]Cochran, T.H., and Masica, W.J., "An Investigation of Gravity Effects on Laminar Gas Jet Diffusion Flames," *Thirteenth Symposium (International) on Combustion*, The Combustion Institute, Pittsburgh, 1970, pp. 821-829.

[2]Haggard, J.B. Jr., and Cochran, T.H. "Stable Hydrocarbon Diffusion Flames in a Weightless Environment," Combust. Sci. Tech., Vol. 5, 1972, pp. 291-298

[3]Edelman, R.B., Fortune, O.F., Weilerstein, G., Cochran, T.H., and Haggard, J.B., Jr., "An Analytical and Experimental Investigation of Gravity Effects upon Laminar Gas Jet-Diffusion Flames," *Fourteenth Symposium (International) on Combustion*, The Combustion Institute, Pittsburgh, 1972, pp. 399-412.

[4]Klajn, M., and Oppenheim, A.K., "Influence of Exothermicity on the Shape of a Diffusion Flame," *Nineteenth Symposium (International) on Combustion*, The Combustion Institute, Pittsburgh, 1982, pp. 223-235.

[5]Edelman, R.B., and Bahadorri, M.Y., "Effects of Buoyancy on Gas-Jet Diffusion Flames: Experiment and Theory," Acta Astronautica ,Vol. 13, 1986, 681-688.

[6]Bahadori, M.Y., Edelman, R.B., Stocker, D.P., and Olson, S.L., "Ignition and Behavior of Laminar Gas-Jet Diffusion Flames in Microgravity," AIAA J., Vol. 28, 1990, pp. 236-244.

[7]Bahadori, M. Y., Stocker, D. P., and Edelman, R. B., "Effects of Pressure on Microgravity Hydrocarbon Diffusion Flames," AIAA Paper No. 90-0651, 1990.

[8]Bahadori, M.Y., Edelman, R.B., Stocker, D.P., Sotos, R.G., and Vaughan, D.F., "Effects of Oxygen Concentration on Radiative Loss from Normal-Gravity and Microgravity Methane Diffusion Flames," AIAA Paper No. 92-0243, 1992.

[9]Faeth, G. M., "Homogeneous Premixed and Nonpremixed Flames in Microgravity: A Review," *Proceedings of the AIAA/IKI Microgravity Science Symposium*, AIAA, Washington, 1991, pp. 281-293.

[10]Glassman, I., "Soot Formation in Combustion Processes," *Twenty-Second Symposium (International) on Combustion*, The Combustion Institute, Pittsburgh, 1988, pp. 295-311.

[11]Schug, K.P., Manheimer-Timnat, Y., Yaccarino, P., and Glassman, I., "Sooting Behavior of Gaseous Hydrocarbon Diffusion Flames and the Influence of Additives," Combust. Sci. Tech.. Vol. 22, 1980, pp. 235-250.

[12]Santoro, R.J., Semerjian, H.B., and Dobbins, R.A., "Soot Particle Measurements in Diffusion Flames," Combust. Flame, Vol. 51, 1983, pp. 203-218.

[13]Santoro, R.J., Yeh, T.T., Horvath, J.J., and Semerjian, H.G., "The Transport and Growth of Soot Particles in Laminar Diffusion Flames," Combust. Sci. Tech., Vol. 53, 1987, pp. 89-115.

[14]Dobbins, R.A., and Megaridis, C.M. "Morphology of Flame-Generated Soot as Determined by Thermophoretic Sampling," Langmuir, Vol. 3, 1987, pp. 254-259.

[15]Megaridis, C.M., and Dobbins, R.A., "Comparison of Soot Growth and Oxidation in Smoking and Nonsmoking Ethylene Diffusion Flames," Combust. Sci. Tech., Vol. 66, 1989, pp. 1-16.

[16]Megaridis, C.M., and Dobbins, R.A., "Morphological Description of Flame-Generated Materials," Combust. Sci. Tech., Vol. 77, 1990, pp. 95-109.

[17]Dobbins, R.A., Santoro, R.J., and Semerjian, H.G., "Analysis of Light Scattering from Soot Using Optical Cross Sections for Aggregates," *Twenty-Third Symposium (International) on Combustion*, The Combustion Institute, Pittsburgh, 1990, pp. 1525-1532.

[18]Puri, R., Richardson, T.F., Santoro, R.J., and Dobbins, R.A., "Aerosol Dynamic Processes of Soot Aggregates in a Laminar Ethene Diffusion Flame," Combust. Flame, in press.

[19]Flower, W.L., and Bowman, C.T., "Measurements of the Structure of Sooting Laminar Diffusion Flames at Elevated Pressures," *Twentieth Symposium (International) on Combustion*, The Combustion Institute, Pittsburgh, 1984, pp. 1035-1044.

[20]Flower, W.L., and Bowman, C.T., "Soot Production in Axisymmetric Laminar Diffusion Flames at Pressures from One to Ten Atmospheres," *Twenty-First Symposium (International) on Combustion*, The Combustion Institute, Pittsburgh, 1986, pp. 1115-1124.

[21]Rogg, B., "On Numerical Analysis of Two-Dimensional, Axisymmetric, Laminar Jet Diffusion Flames," *Mathematical Modeling in Combustion and Related Topics* (C.-M. Brauner and C. Schmidt-Laine, eds.), Martinus Nijhoff Publishers, Amsterdam, 1988, pp. 551-560.

[22]Smooke, M.D., Mitchell, R.E., and Keyes, D.E., "Numerical Solution of Two-Dimensional Axisymmetric Laminar Diffusion Flames," Combust. Sci. Tech., Vol. 67, 1989, pp. 85-122.

[23]Bilger, R. W., "Reaction Rates in Diffusion Flames," Combust. Flame, Vol. 30, 1977, pp. 277-284.

[24]Gore, J.P., and Faeth, G.M., "Structure and Spectral Radiation Properties of Turbulent Ethylene/Air Diffusion Flames," *Twenty-First Symposium (International) on Combustion*, The Combustion Institute, Pittsburgh, 1986, pp. 1521-1531.

[25]Gore, J.P., and Faeth, G.M., "Structure and Radiation Properties of Luminous Turbulent Acetylene/Air Diffusion Flames," J. Heat Trans., Vol. 110, 1988, pp. 173-181.

[26]Sivathanu, Y.R., and Faeth, G.M., "Generalized State Relationships for Scalar Properties in Nonpremixed Hydrocarbon/Air Flames," Combust. Flame, Vol. 82, 1990, pp. 211-230.

[27]Markstein, G. H., "Radiative Energy Transfer from Turbulent Diffusion Flames," Combust. Flame, Vol. 27, 1976, pp. 51-63.

[28]Patankar, S.V., *Numerical Heat Transfer and Fluid Flow*, McGraw-Hill, New York, 1980.

[29]Sivathanu, Y.R., and Faeth, G.M., "Soot Volume Fractions in the Overfire Region of Turbulent Diffusion Flames," Combust. Flame, Vol. 81, 1990, pp. 133-149.

[30]Köylü, Ü.Ö., and Faeth, G.M., "Carbon Monoxide and Soot Emissions from Liquid-Fueled Buoyant Turbulent Diffusion Flames," Combust. Flame, Vol. 87, 1991, pp. 61-76.

[31]Spalding, D. B., *Combustion and Mass Transfer*, Pergamon Press, New York, 1979, Chapt. 10.

[32]Köylü, Ü. Ö., and Faeth, G.M., "Radiative Properties of Flame-Generated Soot," J. Heat Trans., in press.

[33]Köylü, Ü.Ö., and Faeth, G.M., "Optical Properties of Overfire Soot in Buoyant Turbulent Diffusion Flames at Long Residence Times," J. Heat Trans., submitted.

[34]Köylü, Ü.Ö., and Faeth, G.M., "Optical Properties of Soot in Buoyant Laminar Diffusion Flames," 1993 ASME/AIChE National Heat Transfer Conference, Atlanta, Georgia, submitted.

[35]Dalzell, W.H., and Sarofim, A.F., "Optical Constants of Soot and Their Application to Heat Flux Calculations," J. Heat Trans., Vol. 91, 1969, pp. 100-104.

[36]Köylü, Ü.Ö., and Faeth, G.M., "Structure of Overfire Soot in Buoyant Turbulent Diffusion Flames at Long Residence Times," Combust. Flame, Vol. 89, 1992, pp. 140-156.

[37]Rosner, D.E., Mackowski, D.W., and Garcia-Ybarra, P., "Size- and Structure-Insensitivity of the Thermophoretic Transport of Aggregated Soot Particles," Combust. Sci. Tech., Vol. 80, 1991, pp. 87-101.

Table 1 Laminar smoke point luminosity lengths (mm)[a]

Buoyancy State	d (mm)	Pressure (atm) 0.5	1.0	2.0
Ethylene/air flames:				
μg	1.6	80	32	---
μg	2.7	80	25	10
μg	5.9	100	24	10
ng	10.0	---	106-135	---
Propane/air flames:				
μg	1.6	130	42	16
μg	2.7	140	38	18
μg	5.9	130	42	20
ng	10.0	---	162-169	---

[a]Determined for round laminar jet diffusion flames in still air for μg tests; from Schug et al.[11] and Sivathanu and Faeth[29] in coflowing air for ng conditions.

Table 2 Test flames for soot property measurements[a]

Pressure (atm)	0.125	0.188	0.250
Fuel flow rate (mg/s)	3.22	2.64	2.10
Heat release rate (W)	155	127	101
Radiative heat loss fraction (%)	23	28	30
Burner Reynolds number ($u_o d/\nu_o$)	122	100	80
Burner Froude number (u_o^2/gd)	260	77	28
Measurement range (x/d)	4.8-11.5	2.9-12.5	1.9-13.4

[a]Round laminar jet diffusion flames of acetylene in a weak air coflow, 3 mm burner diameter, luminous flame length roughly 60 mm.

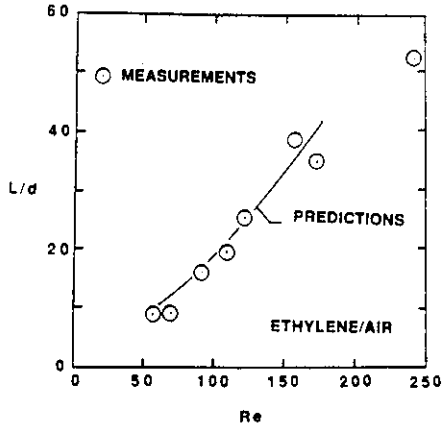

Fig. 1 Predicted and measured flame lengths of nonbuoyant ethylene/air round jet diffusion flames. Measure-ments from Haggard and Cochran.[2]

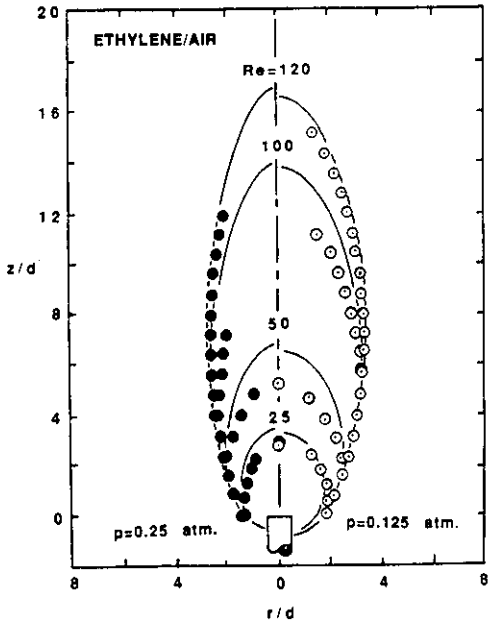

Fig. 2 Predicted and measured flame shapes of weakly-buoyant ethylene/air jet diffusion flames.

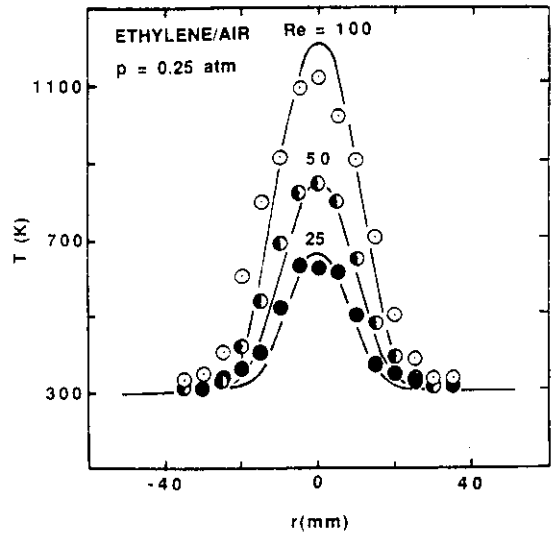

Fig. 3 Predicted and measured temperature distributions in weakly-buoyant ethylene/air jet diffusion flames.

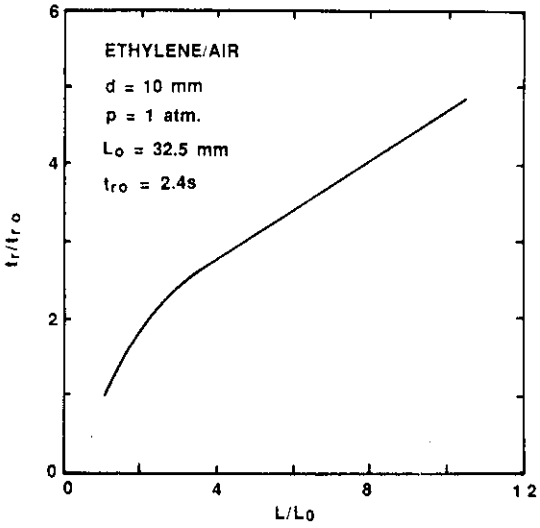

Fig. 4 Predicted flame residence times as a function of flame length for nonbuoyant ethylene/air jet diffusion flames.

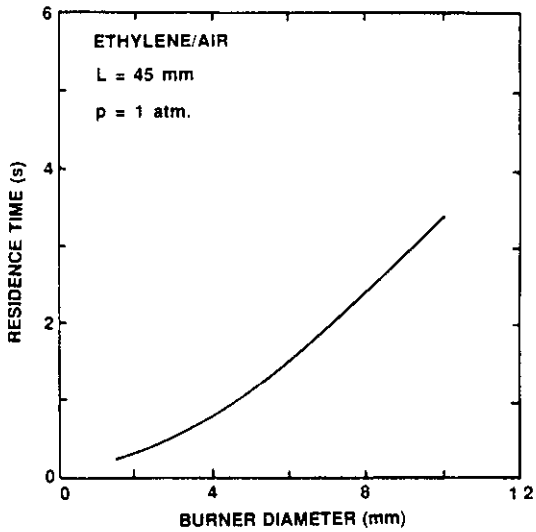

Fig. 5 Predicted flame residence times as a function of burner diameter for nonbuoyant ethylene/air jet diffusion flames.

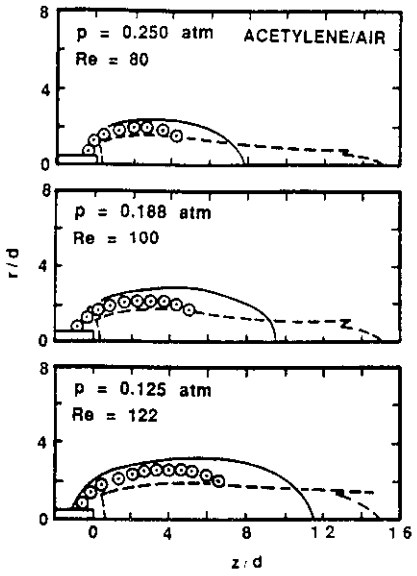

Fig. 6 Flame and luminosity boundaries for the weakly-buoyant acetylene/air test flames.

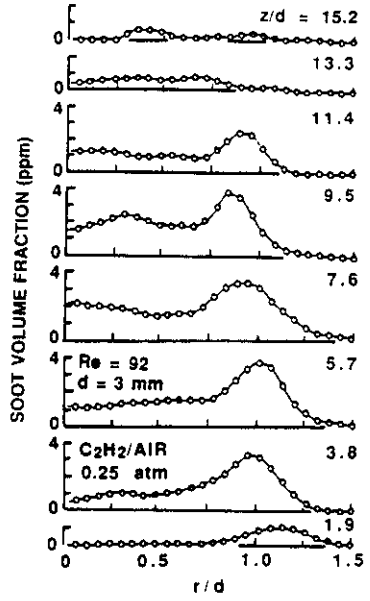

Fig. 7 Measured soot volume fraction distributions for the weakly-buoyant acetylene/air flame at 0.25 atm.

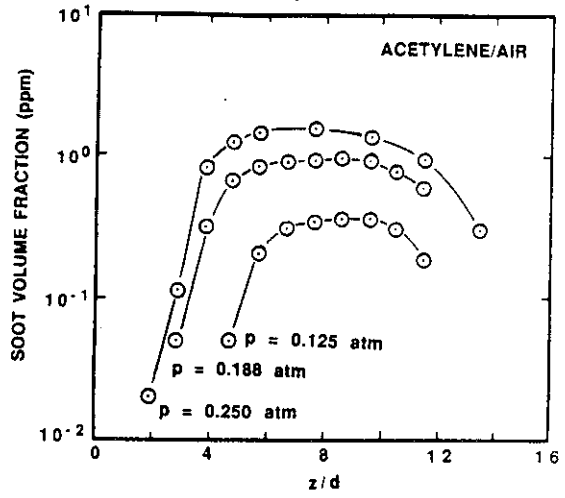

Fig. 8 Soot volume fraction distributions along the axis of weakly-buoyant acetylene/air flames.

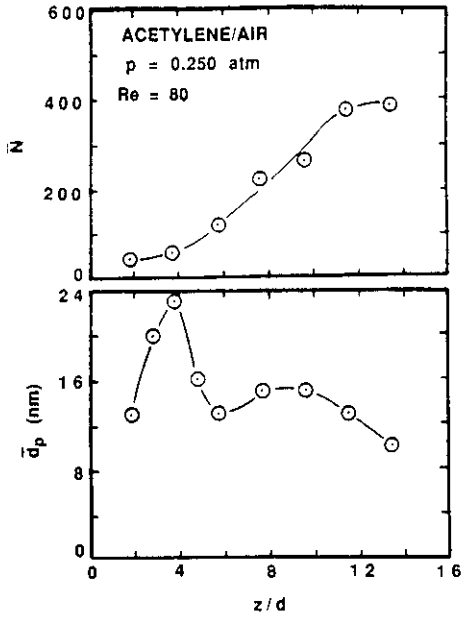

Fig. 9 Soot structure parameters along the axis of the weakly-buoyant acetylene/air flame at 0.25 atm.

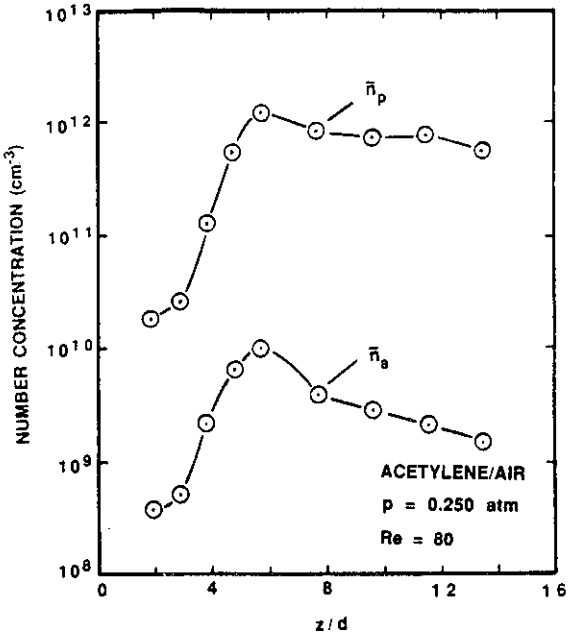

Fig. 10 Primary particle and aggregate concentrations along the axis of the weakly-buoyant acetylene/air flame at 0.25 atm.